Available online at www.sciencedirect.com

ScienceDirect

Procedia Computer Science 271 (2025) 79–85

Procedia Computer Science

www.elsevier.com/locate/procedia

International Conference on Biomimetic Intelligence and Robotics 2025

Conformable Vision-Based Tactile Sensor with Enhanced Soft Elastomer Design for Palpating Irregular Anatomical Surfaces

Yang Yang[a,b], Tao Zhang[a], Yupeng Wang[a], Wenchao Yue[a], Tangyou Liu[a], Hongliang Ren[a,*]

[a]*Department of Electronic Engineering, The Chinese University of Hong Kong, Hong Kong, China*
[b]*Department of Mechanics Science and Engineering, Sichuan University, Chengdu, China*

Abstract

Many cartilage tissues in human organs are covered by skin, making it difficult to assess their characteristics through visual observation alone. Tactile sensing can provide complementary information in such scenarios. Vision-based tactile sensors (VBTS) offer ultra-high resolution and are capable of perceiving relatively large contact areas. In this work, we investigate the application of VBTS in surgical robotic palpation tasks. We enhance the existing sensor hardware to improve its compatibility with the uneven and skin-covered surfaces of cartilage tissues. Finite element simulations are conducted to analyze the underlying mechanical interactions of palpation. Furthermore, we integrate the improved sensor with a robotic arm and perform palpation experiments. The results demonstrate that the VBTS effectively captures both shape and stiffness information of the throat region. Compared to the original design, the enhanced sensor module achieves superior tactile perception performance.

© 2025 The Authors. Published by Elsevier B.V.
This is an open access article under the CC BY-NC-ND license (https://creativecommons.org/licenses/by-nc-nd/4.0)
Peer-review under responsibility of the scientific committee of the Proceedings of the 2025 International Conference on Biomimetic Intelligence and Robotics

Keywords: Vision-based Tactile Sensor; Medical Robotics; Robotic Palpation.

1. Introduction

Human organs that are not visible directly by vision due to their covering of skin need to be scanned and/or examined by surgeons. As shown in Fig. 1, the model of the pharyngeal trachea with epithelium covering was simulated. The area of interest, the region of the trachea ring (red box), comprises four tracheal rings, which are commonly used for palpation during tracheostomy procedures. Under visual conditions alone, it is hard to extract protruding tracheal rings. However, with the addition of tactile information, we may identify and localize these tracheal rings by discerning their differences in hardness [1, 2].

* Corresponding author.
E-mail address: hlren@ee.cuhk.edu.hk

1877-0509 © 2025 The Authors. Published by Elsevier B.V.
This is an open access article under the CC BY-NC-ND license (https://creativecommons.org/licenses/by-nc-nd/4.0)
Peer-review under responsibility of the scientific committee of the Proceedings of the 2025 International Conference on Biomimetic Intelligence and Robotics
10.1016/j.procs.2025.10.114

Vision-based tactile sensors (VBTS) have gained increasing attention in robotic tasks, such as manipulation [3, 4], object recognition[5], pose tracking[6], smart car[7], and medical environments[8, 9, 10] because of their ability to provide high-resolution tactile information. These sensors, such as GelSight [11], rely on optical methods to capture detailed surface deformations, enabling robots to estimate contact forces and reconstruct object geometries effectively [12, 13, 14, 15, 16].

However, challenges arise when using VBTS in scenarios involving soft and uneven surfaces, such as the human pharyngeal trachea. Many organs exhibit irregular shapes, with peaks and valleys that may result in incomplete or inaccurate tactile data. This limitation is often due to the design of the gel elastomer layer in sensors like GelSight, which can be thin or relatively stiff, restricting its ability to conform to highly curved or lumpy surfaces. Consequently, critical information in the concave or lower regions may be lost, reducing the effectiveness of these sensors in such environments.

In this work, we focus on the palpation task of the human throat and trachea, using a robotic arm equipped with a VBTS to touch a model of the human throat, obtaining hardness and shape information of that area to provide recommendations for tracheostomy surgery.

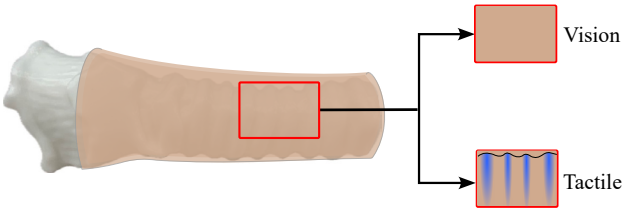

Fig. 1. Simulated throat model covered by rubber skin.

2. Working Principle of Vision-based Tactile Sensor

2.1. Elastomer

In this work, we reproduce a VBTS, called 9DTact[17]. As its hardware and algorithms are open source, we have optimized its materials and structure. The trilayer silicone configuration (transparent, translucent, and black layers) was reengineered to enhance optical performance, mechanical compliance, and biocompatibility for medical applications.

The transparent layer features a dual-functional design, diffusing monochromatic LED illumination to achieve uniform light distribution while suppressing specular reflections through microstructured antireflective features. Notably, unlike conventional photometric stereo sensors that utilize acrylic substrates, this sensor leverages silicone's inherent light scattering properties to mitigate reflection artifacts (see Fig. 2(a))-a critical advantage enabled by our system's direct illumination scheme.

The translucent layer undergoes material substitution and geometric optimization. We replaced the original Posilicone DRSGJ02 with EcoFlex 00-30 to achieve two key improvements: (1) reduced Young's modulus (<0.1MPa) for compliant interaction with soft tissues, and (2) maintained medical-grade biocompatibility. Simultaneously, we increased the layer thickness from 2.5 mm to 4.0 mm to enhance depth sensing capability, which was experimentally validated to provide higher improvement in spatial resolution compared to the original design.

For the black layer, we developed a hybrid formulation using EcoFlex 00-10 with carbon black nanoparticles, which achieves both optical attenuation and environmental light shielding. This layer integration strategy ensures complete encapsulation of the translucent structure while preventing cross-talk between sensing elements. The black layer and translucent layer are shown in Fig. 2 and the final sensor assembly is shown in Fig. 2(d).

2.2. 3D Shape Reconstruction

As shown in Fig. 2(e), the sensor employs a hybrid depth reconstruction methodology tailored for soft tissue exploration. When an object presses against the top black gel layer, the embedded camera system captures pixel

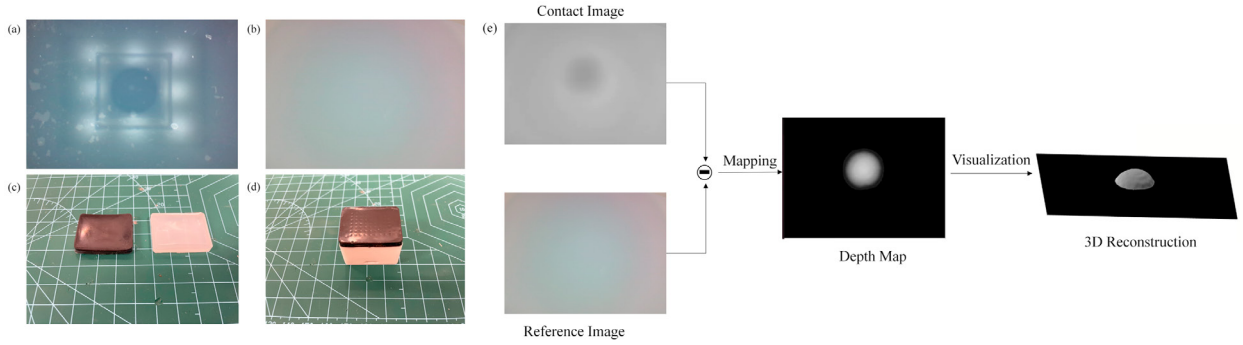

Fig. 2. (a) The reflection phenomenon of acrylic boards; (b) Tactile images when not in contact; (c) Translucent silicone and black silicone; (d) Physical image of the sensor; (e) Principles of 3D shape reconstruction.

intensity variations caused by contact-induced deformation . A baseline reference image is pre-acquired under non-contact conditions to establish pixel intensity distributions for the undeformed state. By subtracting this reference image from the contact image, we isolate pixel intensity variations corresponding to the contact region, highlighting areas of pressure-induced deformation with high contrast. Using a standardized calibration procedure with a known-radius indentation probe (radius $r = 4$ mm), we establish a nonlinear mapping between pixel intensity values and physical indentation depth.

2.3. Finite Element Simulation

To investigate the mechanical behavior of the sensor, we conducted a finite element analysis using ABAQUS[18]. The simulation setup was meticulously designed to replicate the sensor's multi-layer structure and operational conditions. Fig. 3 (a) (b) shows the deformation schematic before and after the ball contacts the silica gel. When the ball touches the sensor, it squeezes the black silica gel downward and around it, and thus, the pixel intensity change is captured by the camera.

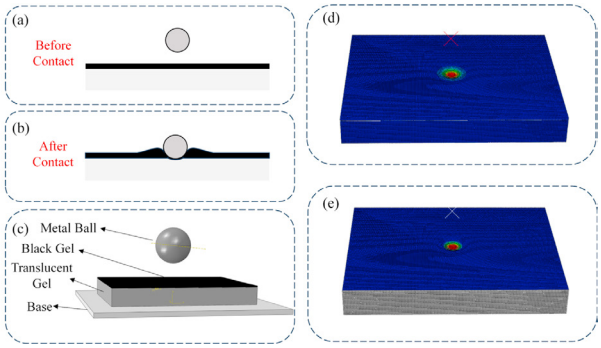

Fig. 3. (a-b) Schematic diagrams of the sensor before and after contact with the object; (c) Simulated assembly diagram; (d) Result contour map of contact displacement; (e) Result contour map of contact force.

1. **Material Modeling** *Transparent Layer*: Encapsulated within the rigid sensor housing and exhibiting negligible deformation (< 0.05 mm) under typical tactile loads, this layer was modeled as a rigid foundation. *Translucent/Black Layers*: Mooney-Rivlin hyperelastic models were employed with parameters calibrated against experimental data from literature [19]. The strain energy function is given by:

$$W = C_1 (I_1 - 3) + C_2 (I_2 - 3) + \frac{1}{D} (J - 1)^2 \tag{1}$$

where C_1, C_2 are Mooney-Rivlin coefficients and D represent the shear modulus.

2. **Mesh Generation** 8-node linear brick elements (C3D8RH) with 0.1 mm edge length were used for both silicone layers to ensure numerical stability in hyperelastic simulations. Hybrid integration and hourglass control were activated to mitigate shear locking. Rigid components (base and indenter) were modeled without mesh discretization, as they exhibited negligible deformation under applied loads.
3. **Boundary Conditions** The base was fully constrained ($u_x = u_y = u_z = 0$, $\omega_x = \omega_y = \omega_z = 0$). The indenter was subjected to a downward displacement of 4 mm at a constant rate of 0.1 mm/step.
4. **Contact Simulation** Binding constraints were applied between adjacent silicone layers to replicate physical adhesion. General contact algorithm was used to model face-to-face interaction between the indenter and black gel layer, accounting for both normal and tangential forces.
5. **Result Analysis** As shown in Fig. 3(d) and (e), the simulation results demonstrate contact displacement and contact force distributions. Similar to actual experiments, when the indenter penetrated the black gel layer by a certain distance, the originally translucent silicone region exhibited black pigment diffusion (Fig. 3(e)). The results preliminarily indicate a linear correlation between contact force and indentation depth.

3. Experiment and Results

3.1. Problem Statement

Tracheostomy surgery typically involves two types of incision locations[20]; one is between the tracheal cartilages and the other is at the cricothyroid membrane. The diagram of the laryngeal tracheal structure is as shown in the Fig. 4(a).

The tracheal cartilage used for localization usually consists of three tracheal rings. Surgeons obtain tactile recognition by palpating the anatomical structures on the surface of the trachea to accurately determine the location of the incision. Generally speaking, the incision is chosen in the softer area between the first and second or the second and third tracheal cartilage rings.

When a patient cannot establish an airway using standard intubation techniques, the cricothyroid membrane is incised, and a tracheal tube is inserted to maintain ventilation; this is known as a cricothyrotomy[21]. This is a crucial emergency procedure, and the primary step of this surgery is locating the cricothyroid membrane, which connects the thyroid cartilage to the cricoid cartilage, as illustrated in the diagram. During clinical operations, doctors typically need to stabilize the trachea with one hand while using the other hand to feel for the Adam's apple and slide down to the dip of the cricothyroid membrane, then they cut in that area and insert the tube. Traditional methods rely on a scalpel and manual exploration. At the same time, robot-assisted technology can integrate specialized tools for more precise and minimally invasive operations, making it particularly suitable for high-pressure environments.

Accurate localization of the cricothyroid membrane is essential and directly determines the success or failure of the surgery. Incorrect localization can result in injury to the cricothyroid artery and tearing of the tracheal cartilage or the formation of a false airway, with complication rates ranging from 10% to 40%, attributed to misidentification of anatomical landmarks[22, 23, 24]. Because this surgery is typically only performed in life-threatening situations where other airway management methods are ineffective, and opportunities for such procedures are rare, medical personnel often face surgical failures due to a lack of sufficient anatomical knowledge or inadequate proficiency. In this paper, we focus simultaneously on the tactile work of robot-assisted surgeries for these two procedures, using a Touch Device equipped with VBTS on a UR5 robotic arm to acquire information on the shape and hardness of the throat.

3.2. Experiment

We utilize the Geomagic Touch Device to remotely control the UR5e robotic arm to perform tactile examination experiments with a tactile sensor, as shown in Fig. 4(b). The model used in the experiment is an adult-sized trachea model, secured to a 3D-printed board with glue, and wrapped in a layer of soft rubber skin. Compared to the Teach Pendant, the Touch Device can achieve a frequency of 125Hz, allowing for smooth operation of the robotic arm. Furthermore, remote operation enables the robotic arm to touch the throat model from all directions, ensuring that as

much tactile information as possible is obtained for subsequent tracheostomy surgery. The VBTS is mounted at the end of the robotic arm, powering the LED light board and driving the camera on the computer to achieve real-time acquisition of tactile images. At this point, the computer can update the contact results in real time and output both point cloud data and contact depth data. Starting from the upper end of the throat, the palpation work is carried out, pausing for a few seconds after each downward touch to ensure stability in tactile imaging while recording point cloud data. After touching downwards 5-7 times from top to bottom, information from the entire area of the throat model can be obtained.

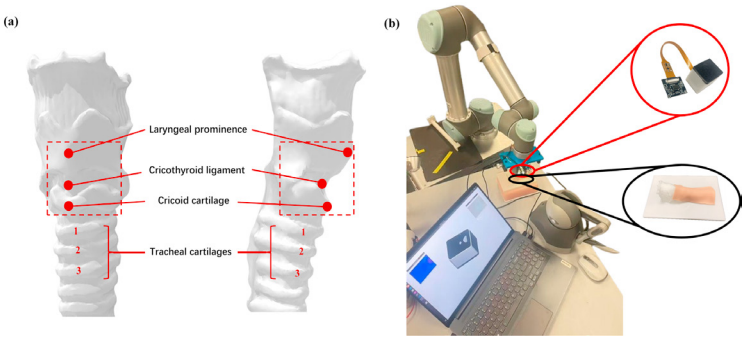

Fig. 4. (a) Anatomical diagram of the throat model; (b) Diagram of the experiment setup

Through seven touches, the area of the throat has been basically covered, as shown in Fig. 5 (b). The dashed box in the upper left corner indicates the direction of palpation, corresponding to the shape reconstruction results obtained from the seven touches. The tactile sensor can accurately reconstruct the laryngeal prominence, cricoid cartilage, and tracheal rings in the throat model, thus providing surgical insertion point suggestions for doctors. The red areas in the figure represent the protrusions in the throat area; the improved vision-based tactile sensor can simultaneously perceive the three tracheal rings and the recessed area between them. Fig. 5 (a) displays the hardness distribution results; according to medical knowledge, the area between each tracheal ring is softer, corresponding to the position between the two red areas in the figure, indicating that the visual tactile sensor can provide medical suggestions for the insertion points of throat trachea surgeries. References [21] and [1]respectively used force sensors to palpate the area of the cricothyrotomy, and dynamic tactile sensors estimated the stiffness of the three tracheal rings. In this paper, we utilize a VBTS to simultaneously accomplish the tasks of both surgeries, obtaining shape and stiffness information of the trachea. Moreover, the visuo-tactile sensor can reconstruct the throat model comprehensively, not limited to collecting information along the midline position. In surgical scenarios, the patient may not be lying flat on the hospital bed, meaning the throat model may not be directly facing the sensor. After remotely operating the UR5 robotic arm using the Touch Device, equipped with the VBTS, the robot is able to perform palpation from multiple angles.

Based on 9DTact, we enhanced the perception unit of the haptic sensor by utilizing silicone of varying thicknesses and hardnesses to make it more suitable for surgical palpation scenarios. As shown in the Table. 1, Type A is the original sensor, with the translucent silicone layer made of Posilicone, a thickness of 2.5 mm, and the black silicone layer made of EcoFlex 00-30, with a thickness of 0.3 mm; whereas Type B is the improved sensor, which, compared to Type A, has a thicker and softer perception body, with the thickness of the translucent layer increased to 4.0 mm and using a softer EcoFlex 00-30, while the black silicone layer also uses a softer EcoFlex 00-10, but the thickness remains unchanged, as a thicker layer reduces sensing capability, so the original thickness was preserved.

We utilize the two sensors to conduct palpation experiments, resulting in a total of 21 touches and 21 point cloud data sets. The chamfer distance was used as the basis for the reconstruction effect:

$$D_{\mathrm{CD}}(S,T) = \frac{1}{2}\left(\frac{1}{|S|}\sum_{s\in S}\min_{t\in T}\|\boldsymbol{s}-\boldsymbol{t}\|_2 + \frac{1}{|T|}\sum_{t\in T}\min_{s\in S}\|\boldsymbol{t}-\boldsymbol{s}\|_2\right) \tag{2}$$

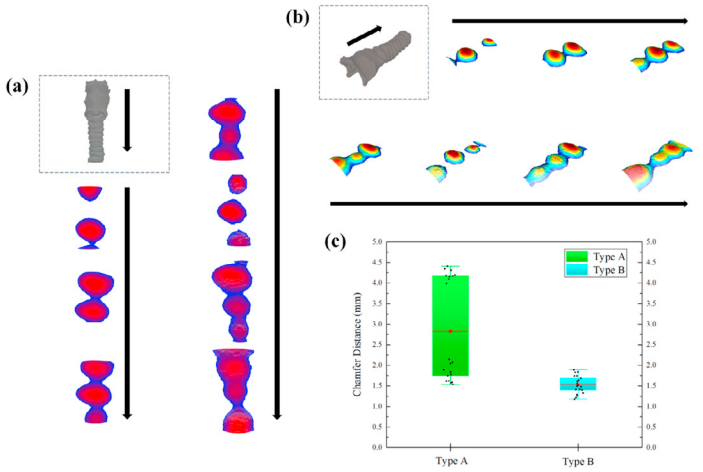

Fig. 5. (a) Hardness map; (b) 3D reconstructed point cloud; (c) Error box plot

in which, S is the source point cloud collection, and T is the target point cloud collection, $|cdot|_2$ denotes the Euclidean distance. Point cloud data exported from an STL file is used as the true value.

Table 1. Silicone materials and geometric parameters of two types of perception modules.

Type of Sensors	Translucent Layer	Black Layer
Type A	2.5 mm Posilicone	0.3 mm EcoFlex 00-30
Type B	4.0 mm EcoFlex 00-30	0.3 mm EcoFlex 00-10

The results are shown in Fig. 5(c), displaying the box plot and scatter plot of 21 touch results from two types of sensors, where the average error of Type A is 2.82 mm and the average error of Type B is 1.53 mm. Furthermore, it can be seen that in the results of Type A, there are some data points that are much larger than the average value; these results come from the dashed box in Fig. 4(a). In these areas, the amplitudes of the fluctuations are significant, and the original 9DTact was unable to effectively sense these uneven regions simultaneously, resulting in larger errors. Type B uses a thicker silicone layer, which can better sense these areas with greater fluctuations. The experimental results demonstrate that the improved sensor can effectively capture all information from the throat area, providing better palpation recommendations for subsequent surgeries.

4. Conclusion

In this paper, we explore the application potential of VBTS in surgical palpation. We focus on the scene of soft cartilage organs covered by the epidermis, particularly in the pharyngeal-tracheal region. This area has some undulating structures that prevent the sensor from capturing the required tactile information in a comprehensive way. Therefore, we modified the perception module of the 9DTact sensor to make it better suited for this palpation task, allowing it to sense both protruding and recessed areas simultaneously. In addition, to better understand the mechanical principles of the sensor, we performed a finite element simulation to obtain contact displacement and contact force cloud maps. We also performed palpation experiments using a Touch Device to remotely operate a UR5e robotic arm equipped with a vision-based tactile sensor, resulting in hardness maps and three-dimensional point clouds of the throat model. We compared the reconstruction results before and after modifications to the sensor. In conclusion, VBTS has broad application prospects in the surgical field and exhibits excellent performance in palpation tasks.

Acknowledgements

This work was supported in part by Hong Kong Research Grants Council (RGC) Collaborative Research Fund (CRF C4026-21GF), Research Impact Fund (RIF R4020-22), General Research Fund (GRF 14216022, GRF 14203323, GRF 14204524), Guangdong Basic, Applied Basic Research Foundation (GBABF) #2021B1515120035 and, the National Academy of Medicine (NAM) of the United States and Hong Kong Research Grants Council (RGC) Health Longevity Catalyst Awards (grant no. HLCA/E-403/22); CUHK Faculty Direct Grant (4055213) and Shenzhen-Hong Kong-Macau Technology Research Programme (Type C) (grant no. 202108233000303).

References

[1] W. Yue, F. Bai, J. Liu, F. Ju, M. Q.-H. Meng, C. M. Lim, and H. Ren, "Rasec: Rescaling acquisition strategy with energy constraints under fusion kernel for active incision recommendation in tracheotomy," *IEEE Transactions on Automation Science and Engineering*, 2024.

[2] T. Liu, X. Zhang, C. Zhang, T. Wang, S. Song, J. Wang, and L. Wu, "Robotic intracorporeal palpation with a miniature force-sensing probe for minimally invasive surgery," *IEEE Transactions on Instrumentation and Measurement*, 2025.

[3] M. Bauza, A. Bronars, Y. Hou, I. Taylor, N. Chavan-Dafle, and A. Rodriguez, "Simple, a visuotactile method learned in simulation to precisely pick, localize, regrasp, and place objects," *Science Robotics*, vol. 9, no. 91, p. eadi8808, 2024.

[4] T. Liu, X. Wang, J. Katupitiya, J. Wang, and L. Wu, "Automatic tissue traction using miniature force-sensing forceps for minimally invasive surgery," *IEEE Transactions on Robotics*, 2024.

[5] J. Xu, H. Lin, S. Song, and M. Ciocarlie, "Tandem3d: Active tactile exploration for 3d object recognition," in *2023 IEEE International Conference on Robotics and Automation (ICRA)*. IEEE, 2023, pp. 10 401–10 407.

[6] H.-J. Huang, M. Kaess, and W. Yuan, "Normalflow: Fast, robust, and accurate contact-based object 6dof pose tracking with vision-based tactile sensors," *IEEE Robotics and Automation Letters*, 2024.

[7] S. Li, J. Xu, T. Wu, Y. Yang, Y. Chen, X. Wang, W. Ding, and X.-P. Zhang, "Vtire: A bimodal visuotactile tire with high-resolution sensing capability," *IEEE/ASME Transactions on Mechatronics*, 2025.

[8] S. Cui, Y. Tian, J. Hu, R. Wang, Y. Wang, and S. Wang, "Prototype of a novel visuotactile endoscope probe," in *2023 IEEE 13th International Conference on CYBER Technology in Automation, Control, and Intelligent Systems (CYBER)*. IEEE, 2023, pp. 1368–1373.

[9] J. Di, Z. Dugonjic, W. Fu, T. Wu, R. Mercado, K. Sawyer, V. R. Most, G. Kammerer, S. Speidel, R. E. Fan *et al.*, "Using fiber optic bundles to miniaturize vision-based tactile sensors," *arXiv preprint arXiv:2403.05500*, 2024.

[10] W. Li, Z. Zhao, L. Cui, W. Zhang, H. Liu, L.-A. Li, and Y. Zhu, "Minitac: An ultra-compact 8 mm vision-based tactile sensor for enhanced palpation in robot-assisted minimally invasive surgery," *IEEE Robotics and Automation Letters*, 2024.

[11] W. Yuan, S. Dong, and E. H. Adelson, "Gelsight: High-resolution robot tactile sensors for estimating geometry and force," *Sensors*, vol. 17, no. 12, p. 2762, 2017.

[12] E. Donlon, S. Dong, M. Liu, J. Li, E. Adelson, and A. Rodriguez, "Gelslim: A high-resolution, compact, robust, and calibrated tactile-sensing finger," in *2018 IEEE/RSJ International Conference on Intelligent Robots and Systems (IROS)*. IEEE, 2018, pp. 1927–1934.

[13] A. Alspach, K. Hashimoto, N. Kuppuswamy, and R. Tedrake, "Soft-bubble: A highly compliant dense geometry tactile sensor for robot manipulation," in *2019 2nd IEEE International Conference on Soft Robotics (RoboSoft)*. IEEE, 2019, pp. 597–604.

[14] C. Lin, Z. Lin, S. Wang, and H. Xu, "Dtact: A vision-based tactile sensor that measures high-resolution 3d geometry directly from darkness," in *2023 IEEE International Conference on Robotics and Automation (ICRA)*. IEEE, 2023, pp. 10 359–10 366.

[15] B. Ward-Cherrier, N. Pestell, L. Cramphorn, B. Winstone, M. E. Giannaccini, J. Rossiter, and N. F. Lepora, "The tactip family: Soft optical tactile sensors with 3d-printed biomimetic morphologies," *Soft robotics*, vol. 5, no. 2, pp. 216–227, 2018.

[16] T. Liu, T. Zhang, J. Katupitiya, J. Wang, and L. Wu, "Haptics-enabled forceps with multimodal force sensing: Toward task-autonomous surgery," *IEEE/ASME Transactions on Mechatronics*, vol. 29, no. 3, pp. 2208–2219, 2023.

[17] C. Lin, H. Zhang, J. Xu, L. Wu, and H. Xu, "9dtact: A compact vision-based tactile sensor for accurate 3d shape reconstruction and generalizable 6d force estimation," *IEEE Robotics and Automation Letters*, 2023.

[18] S. Helwany, *Applied soil mechanics with ABAQUS applications*. John Wiley & Sons, 2007.

[19] L. Marechal, P. Balland, L. Lindenroth, F. Petrou, C. Kontovounisios, and F. Bello, "Toward a common framework and database of materials for soft robotics," *Soft robotics*, vol. 8, no. 3, pp. 284–297, 2021.

[20] H. Gray, *Anatomy of the human body*. Lea & Febiger, 1878, vol. 8.

[21] N. Shihora, R. Yasin, R. Walsh, and N. Simaan, "Feasibility of remote landmark identification for cricothyrotomy using robotic palpation," in *2021 IEEE/RSJ International Conference on Intelligent Robots and Systems (IROS)*. IEEE, 2021, pp. 1808–1814.

[22] D. Elliott, P. Baker, M. Scott, C. Birch, and J. Thompson, "Accuracy of surface landmark identification for cannula cricothyroidotomy," *Anaesthesia*, vol. 65, no. 9, pp. 889–894, 2010.

[23] L. White, R. A. Bly, D. D'Auria, N. Aghdasi, P. Bartell, L. L. Cheng, and B. Hannaford, "Cricothyrotomy simulator with computational skill assessment for procedural skill training in the developing world," *Otolaryngology—Head and Neck Surgery*, vol. 149, no. 2_suppl, pp. P60–P60, 2013.

[24] K. L. Hart and S. H. Thompson, "Emergency cricothyrotomy," *Atlas of the oral and maxillofacial surgery clinics of North America*, vol. 18, no. 1, pp. 29–38, 2010.